This is a repository copy of *Using Ag nanoparticles in the electron transport layer of perovskite solar cells to improve efficiency*.

White Rose Research Online URL for this paper:
https://eprints.whiterose.ac.uk/220613/

Version: Published Version
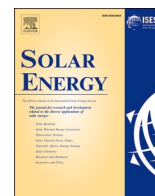
Article:

Using Ag nanoparticles in the electron transport layer of perovskite solar cells to improve efficiency

Francesco Bastianini [a],[*], Ana Isabel Casas Hidalgo [a], Daniel Z. Hook [b], Joel A. Smith [b], Denis Cumming [a], Alan Dunbar [a]

[a] *Department of Chemical and Biological Engineering, The University of Sheffield, Mappin Street, Sheffield S1 3JD, UK*
[b] *Department of Physics and Astronomy, The University of Sheffield, Hounsfield Road, Sheffield S3 7RH, UK*

A B S T R A C T

The incorporation of metal nanoparticles within various types of photovoltaic technologies has been shown to increase the performance of organic solar cells, dye sensitized solar cells, and more recently perovskite solar cells. Using this type of nanostructured composite transport layer could help improve the efficiency and stability of perovskite solar cells whilst avoiding the use of dopants that can damage the perovskite layer. In this work, Ag nanoparticles are synthesized and used to form a SnO$_2$:Ag nanoparticle composite transport layer for the first time. On its own, SnO$_2$ is in one of the most efficient transport layers for perovskite solar cells. Upon inclusion of the Ag nanoparticles the recombination rate is increased (detrimental for device performance) as shown by impedance spectroscopy, and the charge carrier transfer and extraction is enhanced (beneficial for device performance) as shown by photoluminescence measurements. In order to balance these opposing factors, the nanoparticle concentration was optimized at an intermediate concentration with a corresponding power conversion efficiency increase from 13.4 ± 0.7 % for reference solar cells without nanoparticles to 14.3 ± 0.3 % for those with nanoparticles. These devices are one of the first examples of, and exhibit the highest reported efficiency for, perovskite solar cells fabricated completely in air with nanocomposite oxide layers. The protocol developed and reported here to improve the nanocomposite transport layer has general applicability in other fields, including LEDs, FETs, and electronic devices where transparency and conductivity are also required.

1. Introduction

In recent years, the world of photovoltaics has been revolutionized by the rapid development of a new technology: perovskite solar cells based on halide perovskites. Since their first application in dye sensitized solar cells with an efficiency of 3.8 % by Miyasaka *et al.* in 2009, [1] perovskite solar cells have experienced unprecedented performance gains, reaching efficiencies of 26.1 % in 2023.[2] The interest in and the successful rise of perovskites can be ascribed to their low cost associated with both cheap, abundant materials and processing via economical methods in solution (T ≤ 100 °C), as well as to their excellent photovoltaic properties: extremely high absorbance,[3] high electron and hole mobilities,[4] and good tolerance towards defects.[5] However, for widespread adoption of perovskite solar cells into the solar cell market several outstanding issues must first be resolved. Firstly, their sensitivity towards O$_2$, H$_2$O, UV light and high temperatures both during deposition necessitating expensive control of the processing environment

(efficiency in ambient air is limited to ≈20 %[6]) and during operation. Secondly, the upscaling to large area devices, and thirdly the lack of suitable transport layers.[7,8] In particular, the highest efficiencies in perovskite solar cells have been obtained by employing expensive transport layers, that contain dopants that are known to degrade the perovskite layer.[8–12] Progress in developing inexpensive undoped transport layers is of great relevance for perovskite solar cell development.

Following methods used by the organic photovoltaics and dye sensitized solar cells communities, it is possible to identify a strategy to enhance the performance of the transport layers: thanks to the creation of composite transport layers with metal nanoparticles, the efficiencies of organic solar cells have been increased by 15–70 % [13] with respect to the efficiency of devices without nanoparticles. Only a few works have been reported for nanoparticles within perovskite solar cells. [14–18] However, these do not cover all the varieties of possible transport layers; in particular, addition of nanoparticles has never been

reported for one of the most successful electron transport layers, SnO_2. Additionally, the most commonly employed technique to produce the nanoparticles to be incorporated into the charge transport layers is chemical synthesis, with only a few studies involving other techniques, *e.g.*, thermal evaporation, electron beam evaporation, sputtering, and laser ablation.[19].

Several phenomena have been identified as possible mechanisms for the improvement of the performance of solar cells incorporating nanoparticles, and sometimes several of these mechanisms may be occurring simultaneously. The most commonly reported are: (1) the embedded nanoparticles increase the roughness and the surface area of the transport layers, thus providing better adhesion with the overlying active layer, and consequently an enhanced extraction of charge carriers;[20] (2) the metal nanoparticles increase the conductivity of charge carriers through the transport layer, whereas the blocking of opposite charge carriers should be guaranteed by a full covering of the transport layer around the surface of the nanoparticles;[21] (3) beneficial optical effects due to the metal nanoparticles. In particular, large nanoparticles (>40 nm) scatter the light into the absorber layer, therefore increasing the optical path of the light within the absorber increasing the probability of absorbance, whereas small nanoparticles (<40 nm) exhibit localized surface plasmonic resonance (LSPR).[22] In this case, the nanoparticles act as antennae, that trap the light in their proximity, and if the absorbing layer is located within a few tens of nm from the nanoparticles, this highly localized electromagnetic field can directly excite electrons into the conduction band, initiating the photovoltaic effect. [19].

In this work, Ag nanoparticles will be integrated into the SnO_2 electron transport layer of $CH_3NH_3PbI_3$ perovskite solar cells, for the first time. SnO_2 has been selected because it has been used in some of the perovskite solar cells with the highest efficiencies (25.5 % when processed in a glovebox [23]), it can be processed in air at low temperatures (100 °C), and exhibits a good stability. Ag is a very suitable material for nanoparticles due to its facile growth in nanostructured forms, its high conductivity at room temperature, its stability, and its plasmonic effect in the visible region of the spectrum.[24] Unlike other works in the literature, this investigation is not limited to only one nanoparticle preparation technique, but considers both chemical synthesis and physical deposition (via thermal evaporation) in order to compare these techniques and to discover the most suitable for application in photovoltaics. After the characterization of the SnO_2:Ag nanoparticle composite layers, these will be incorporated into solar cells that are fully fabricated in air. Fabrication in air minimizes their fabrication cost and moves closer to a fabrication method appropriate for industrial production. In this work, Methylammonium Lead Iodide ($CH_3NH_3PbI_3$) is chosen as the light absorbing material for our devices because it is well understood, and consistently results in efficient solar cells. Whilst other multi-cation perovskites can result in higher efficiency devices, it was considered necessary to use this well studied single cation system to ensure that the improvements observed can be reliably attributed to the addition of the nanoparticles. An additional goal of this work is to solve the discussion in the literature about the origin of the improvement in PCE of solar cells after integration of nanoparticles, by understanding the mechanisms by which nanoparticles influence device performance.

2. Experimental methods

2.1. Formation of Ag nanoparticles

Ag nanoparticles are produced either via a physical method (thermal evaporation) or via a chemical reaction. Thermal evaporation is performed with an Edwards Auto 306 metal evaporator, at pressures of 6–8 $\times$ 10^{-6} mbar, with a deposition rate of $\approx$0.1 nm/s, to achieve final thicknesses in the range 0.25–13.9 nm. Ag pellets (99.99 % purity) are evaporated from a Tungsten boat, both from the Kurt J. Lesker Company. For continuous layers above the percolation threshold (>5 nm),

[25,26] a thermal treatment is performed in a tube furnace in air for 20 min at temperatures 100–400 °C, in order to promote the rearrangement into a discontinuous nanoparticle layer. Chemical synthesis of Ag nanoparticles is achieved by reaction of 0.002 M $AgNO_3$ (Alfa Aesar) and 0.001 M $NaBH_4$ (Sigma Aldrich) in DI H_2O.[27] After the reaction, polyvinyl pyrrolidone (PVP, Sigma Aldrich, MW = 10 000) is added as a capping layer for Ag nanoparticles.[27].

2.2. Ag nanoparticles + SnO_2 composite layers

Nanoparticles are incorporated into transport layers with 2 possible topologies: either below or embedded inside the transport layer. The first case is applied for nanoparticles produced by physical methods; the transport layer is spin coated directly on the top of the substrates where the nanoparticles were grown. The second case is suitable for nanoparticles from chemical synthesis; Ag nanoparticle solution and transport layer solution are mixed in different ratios, and co-deposited via spin coating on suitable substrates.

SnO_2 is deposited from a colloidal SnO_2 nanoparticle dispersion in H_2O (15 % concentration), from Alfa Aesar. This colloidal solution is diluted in DI H_2O in a ratio DI H_2O: SnO_2 solution of 4:1 $_{vol}$, then spin coated at 2000 rpm for 30 s, and lastly annealed at 100 °C for 30 min. [28,29] For composite layers from chemical synthesis, the aqueous Ag nanoparticle dispersion partially or completely replaces the H_2O in the dilution step, with ratios 1:1 $_{vol}$, 2:1 $_{vol}$, or 4:1 $_{vol}$ with respect to the volume of SnO_2 solution.

2.3. Fabrication of perovskite solar cells

Solar cells are fabricated with a normal architecture comprising of ITO/SnO_2/$CH_3NH_3PbI_3$/PTAA/Ag as reported in Fig. 1, with all the layers deposited in air. The ITO Glass Photovoltaic Substrates (8 Pixel) are from Ossila Ltd, where the ITO has a thickness of 100 nm, and a nominal sheet resistance of 20 Ω/□. The substrate cleaning protocol applied immediately prior to use is: 10 min ultrasonication in Hellmanex solution (Hellmanex III from Hellma Analytics, $\approx$ 0.5 %$_{vol}$ in boiling DI H_2O); rinsing twice in hot H_2O and once in room temperature H_2O; 10 min ultrasonication in acetone ($\geq$99.5 %, Honeywell); 10 min ultrasonication in isopropanol (Propan-2-ol $\geq$ 99.5 %, Fisher Scientific); drying with N_2 gun; and 5–10 min oxygen plasma cleaning. The first layer to be deposited is SnO_2 (Electron Transport Layer, ETL), either pristine or as a composite with Ag nanoparticles via physical methods or chemical synthesis. $CH_3NH_3PbI_3$ perovskite is deposited via a modification of the antisolvent technique reported in the literature.[30,31] CH_3NH_3I and PbI_2 were synthesized in our lab as reported in the literature,[32,33] and mixed with molar ratio 1:1 in DMF:DMSO 4:1 $_{vol}$ (N, N-dimethylformamide anhydrous, 99.8 % from Sigma Aldrich; dimethyl sulfoxide, analytical reagent grade, from Fisher Scientific UK), in order to have concentration of 1.3 M each. The solution is spin coated under
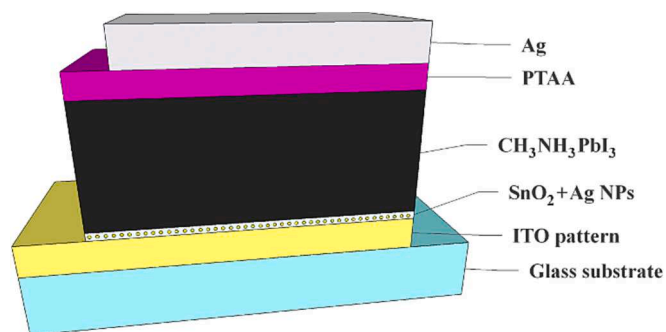

Fig. 1. Architecture of solar cells. Schematic representation of a solar cell, with layers: ITO (100 nm), SnO_2 (24.7 $\pm$ 0.1 nm), $CH_3NH_3PbI_3$ (373 $\pm$ 3 nm), PTAA (72.6 $\pm$ 0.2 nm), Ag (110 nm).

fumehood at 3000 rpm for 20 s, and after 10 s ethyl acetate (anhydrous 99.8 %, Sigma Aldrich) is added as an antisolvent rinse.[31] After the spin coating, the Perovskite samples are first transferred into a small vacuum chamber, and exposed to low vacuum (1.2 mbar) for 2 min. After this vacuum treatment, the samples are annealed at 100 °C for 1 min. This modification aims at depositing perovskite in air with good quality: high crystallinity, full coverage, uniform grains with low roughness, and absence of pinholes. On top of the perovskite layer, a PTAA (Poly-triarylamine, M513 from Ossila Ltd, MW = 28 422) hole transport layer is deposited. PTAA has the advantage of being easily processed in air, therefore suitable for our goal of solar cells fully fabricated in ambient environment. 15 mg/mL of PTAA in toluene (anhydrous 99.8 %, Sigma Aldrich) is doped with Li-TFSI (Lithium bis (trifluoromethylsulfonyl) imide from Ossila Ltd, dissolved with concentration of 170 mg/mL in acetonitrile, VWR Chemicals) and tBP (4-*tert*-Butylpyridine from Ossila Ltd, diluted 1:1 $_{vol}$ in acetonitrile). The volumetric ratio of PTAA solution:Li-TFSI solution:tBP solution is 1000:7.5:7.5. The global solution is deposited statically and spin coated at 3000 rpm for 30 s (modifications from the literature [34–36]), and annealed at 100 °C for 10 min. Lastly, Ag is deposited with the same apparatus for thermal evaporation of Ag nanoparticles, but with thicknesses of 110 nm. For Electrochemical Impedance Spectroscopy measurements, Au (99.99 % purity, Agar Scientific) is thermally evaporated as back electrode, with thickness of 110 nm.

2.4. Characterization

Layer morphology is analyzed by Atomic Force Microscopy (AFM), with a Bruker Dimension Icon ScanAsyst, operating in tapping mode with a nominal frequency of 70 ± 25 kHz, and using silicon nitride ScanAsyst-Air tips. UV–Vis absorbance spectra are acquired with a deuterium - tungsten halogen lamp (250–830 nm) and an Ocean Optics USB 2000 + photodetector. Electrical conductivity is measured via a 4 point probe in line device, with a Keithley 2602A SourceMeter and a voltage sweep from −1 V to 1 V with steps of 0.1 V. Electrochemical Impedance Spectroscopy (EIS) is performed with an IviumStat.h standard instrument with a FRA/EIS analyzer, for frequencies from 100 kHz to 100 mHz, and a bias offset of 0.9 V. Time Resolved Photoluminescence data are acquired using the Time Correlated Single Photon Counting (TCSPC) technique, with a laser of wavelength 510 nm, frequency 40 MHz, and fluency 107 ± 1 μW. For each sample, the wavelength selected for TCSPC was the maximum in the PL spectrum, ≈768 nm. The efficiency of solar cells is measured using a solar simulator Newport 92251A-1000 with a Xenon lamp, applying a mask to the solar cells with active areas of 2.365 ± 0.012 mm^2. Intensity of the light is 1 sun AM1.5G, and the lamp is calibrated before every measurement.

3. Results and discussion

3.1. Production of Ag nanoparticles

3.1.1. Thermal evaporation

As reported in a previous paper by the authors,[37] metal nanoparticles can be grown on inert substrates either directly for deposits thinner than the percolation threshold ($\leq$5 nm), or via thicker deposits (>5 nm) followed by thermal annealing to promote the rearrangement of the continuous layers into discrete nanoparticles. Samples that are thinner than the percolation threshold can also be annealed in order to make the nanoparticles more spherical and to improve the uniformity of the deposit. The annealing is performed in air for 20 min, with temperatures increasing with the thickness of the deposit: 100 °C for 1 nm, 200 °C between 2 nm and 5 nm, and 300 °C between 10 nm and 13.9 nm.

During the growth of a thermally evaporated film it will transition through two regimes which can be monitored by measuring the optical absorption and its electrical properties. Initially, the low amount of incoming metal arranges in a discontinuous nanoparticle film, that is

characterized by an optical absorption peak (centered between 350 nm and 600 nm of Ag nanoparticles) generated by localized surface plasmonic resonance, and at this stage the film is electrically insulating. Later, with the arrival of further material, the nanoparticles coalesce into a continuous metal film where electrons are no longer confined,[38] this continuous film is characterized by a flat absorption spectrum and a long range electrical conductivity.

However, thin continuous films are unstable and with sufficient thermal energy (100–400 °C) they can be rearranged into films with a morphology consisting of large hemispherical nanoparticles, characterized by sharp plasmonic peaks at 430–500 nm. With this strategy, it is possible to achieve nanoparticle layers even above the percolation threshold.

The dimension of the nanoparticles depends on the thickness of the film before the annealing. The plasmonic absorption shifts with the dimensions of the nanoparticles formed after the annealing. Therefore, tuning the deposition conditions (thickness and temperature of annealing) is a convenient method to control the optical properties of the nanoparticle films.
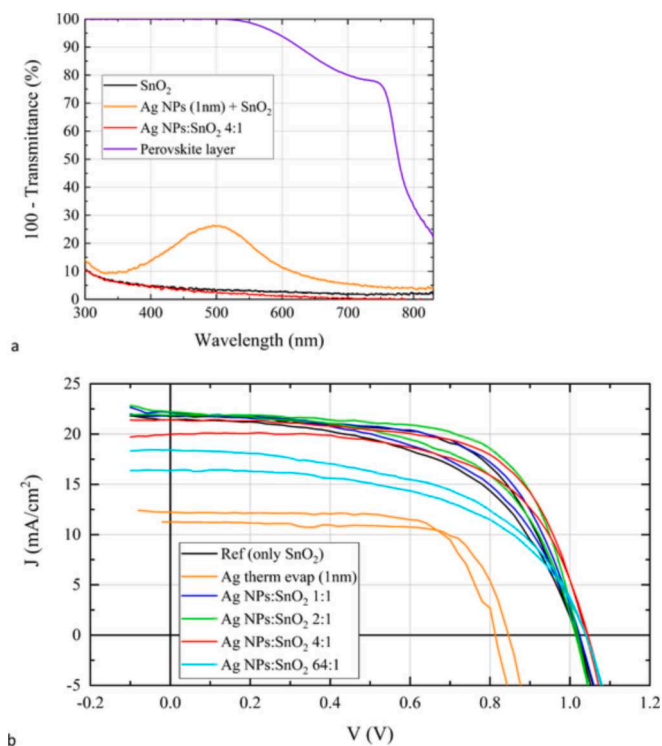
3.1.2. Chemical synthesis of Ag nanoparticles

Ag nanoparticles are synthesized in DI H$_2$O from a Ag salt (AgNO$_3$). A strong reductant (NaBH$_4$) is employed in order to have fast nucleation resulting in small nanoparticles with a narrow distribution in dimensions.[27] AFM measurements detect nanoparticles with an average radius of 8.6 nm, in agreement with Nanoparticle Tracking Analysis (NTA) that reports that almost 50 % of nanoparticles have radii between 5 nm and 10 nm. Their concentration is estimated by NTA to be 9×10^{11} NPs/mL. The plasmonic peak of the Ag nanoparticles in solution is centered at 399.8 ± 0.8 nm. The concentration of nanoparticles is increased via 2 sequential centrifugations at 14 000 rpm for 60 min, for a total increase in concentration by 20 times.

3.2. Integration of Ag nanoparticles into transport layers

Having established suitable parameters to synthesize Ag nanoparticles via physical and chemical methods, the following step is to fabricate composite transport layers by integrating the Ag nanoparticles into the SnO$_2$ layers, and to characterize their optical, electrical and morphological properties. As shown in Fig. 2a, UV–Vis measurements indicate plasmonic absorbance only for composite layers with thermally evaporated nanoparticles, whereas all the composite layers with chemically synthesized nanoparticles are transparent, similar to the SnO$_2$ layer without nanoparticles. The reason for this can be found by analyzing the morphology via AFM. Thermal evaporation forms layers where nanoparticles are close to each other (distances of few nanometers), whereas nanoparticles from chemical synthesis are deposited via spin coating which provides a significantly less dense layer of nanoparticles (distances of tens of nanometers), that is the concentration of Ag nanoparticles present is much smaller in the chemically derived films. Additionally, the roughness of composite layers is enhanced with respect to bare SnO$_2$. Regarding the electrical characterization, the conductivities of SnO$_2$ layers decrease after incorporating Ag nanoparticles, both from thermal evaporation and from chemical synthesis. This can be explained by the difference in work functions, that drives the electrons from SnO$_2$ to Ag. The electron depleted regions in SnO$_2$ decrease the conductivity of the composite layer, in a process similar to the formation of a nano-Schottky barrier.[39,40].

3.3. Integration of Ag nanoparticles into transport layers of perovskite solar cells

Ag nanoparticles are incorporated into perovskite solar cells in 2 ways: Ag nanoparticles thermally evaporated between ITO and SnO$_2$ and Ag nanoparticles from chemical synthesis co-deposited with SnO$_2$. Due to the dimensions of the Ag nanoparticles via chemical synthesis

Fig. 2. J-V graph and UV–Vis spectra. (a) 100 - Transmittance via UV–Vis spectroscopy of bare SnO_2, SnO_2 with Ag nanoparticles via thermal evaporation or chemical synthesis, and perovskite layer. (b) Density of current J - Voltage V graph for reference solar cell ITO / SnO_2 / $CH_3NH_3PbI_3$ / PTAA / Ag (black curve), for solar cell with Ag nanoparticles via thermal evaporation at the interface ITO / SnO_2 layer (violet curve), and for solar cell with Ag nanoparticles via chemical synthesis into the SnO_2 layer with different concentrations (blue, green and red curves). (For interpretation of the references to colour in this figure legend, the reader is referred to the web version of this article.)

(radius 8.6 nm) and via thermal evaporation (radius 10–13 nm), and the thickness of SnO_2 ($\approx$25 nm), the two systems are comparable because the nanoparticles are completely covered by the transport layer material.

Ag nanoparticles thermally evaporated (1 nm, as deposited or annealed at 100 or 200 °C) between ITO and SnO_2 decrease the efficiency of perovskite solar cells by values between −54 % and −80 % with respect to reference solar cells without nanoparticles. This is mainly due to a drop in J_{SC}. J-V curves for the reference solar cell and for the solar cell with 1 nm of Ag as deposited are reported in Fig. 2b. Possible reasons for this decrease include a misalignment of energy levels between the active layer and the transport layer after incorporation of nanoparticles; the competition to absorb light between the plasmonic nanoparticles and the active layer, although UV–Vis analysis (Fig. 2a) determined this effect to be significantly smaller ($\approx$11 %) than the decrease in efficiency (-54 %); and possible recombination of

electrons and holes mediated by nanoparticles.

Ag nanoparticles from chemical synthesis are mixed and co-deposited with SnO_2, so that they are embedded inside the transport layer. The Ag nanoparticle solution partially replaces the DI H_2O used for dilution of SnO_2 solution: the ratios of Ag nanoparticle solution:SnO_2 solution studied are 0:1 (no Ag nanoparticles), 1:1, 2:1, and 4:1 (complete replacement of DI H_2O with Ag nanoparticle solution). J-V curves for the reference solar cell and for the solar cells with the 3 different concentrations of Ag NPs are compared in Fig. 2b. Performance results for the perovskite solar cells with composite transport layers are listed in Table 1, and the main parameters are plotted as a function of nano-particle concentration: PCE (Fig. 3a), V_{OC} (Fig. 3b), J_{SC} (Fig. 3c), and FF (Fig. 3d). Ag nanoparticles made by chemical reaction increase the PCE of perovskite solar cells from 13.4 $\pm$ 0.7 % to 14.3 $\pm$ 0.3 % (relative increase of + 7 %), for nanoparticles with ratio Ag nanoparticle solution: SnO_2 solution 2:1. This increase is due to the simultaneous enhancements of both FF (+8%) and V_{OC} (+1%), whereas J_{SC} decreases slightly. Because the V_{OC} increases with the concentration of Ag nanoparticles, solar cells with even higher concentration were fabricated by further centrifugation of the nanoparticle solution, to achieve equivalent concentration of 64:1 (light blue J-V curve in Fig. 2b). The V_{OC} was effectively increased, but the PCE continued the drop as noted already for 4:1 concentration and reached values below the reference SnO_2, due to decreases in both J_{SC} and FF. Therefore, because the V_{OC} constantly increases whereas the J_{SC} decreases, the highest PCE is achieved at intermediate concentration of 2:1. The different results observed for Ag nanoparticles from thermal evaporation and from chemical synthesis can be explained by the different nanoparticle concentrations: thermal evaporation deposits Ag nanoparticles at a concentration which is too high and sits above the maximum in PCE, whereas the concentration of the chemically derived nanoparticles can be easily tuned. Our results demonstrate that the beneficial effects of adding metal nanoparticles into oxide transport layers in the literature (TiO_2,[14–16,41–45] Al_2O_3, [42,46] MgO,[17] VO_x,[47]) are applicable also for SnO_2. Among these devices, the best solar cells fully fabricated in air reached an efficiency of 13.8 % for Au/SiO_2 core/shell nanoparticles in mesoporous TiO_2.[41] To the best of our knowledge, the PCE of 14.3 $\pm$ 0.3 % for Ag nanoparticles in SnO_2 represents the highest efficiency for solar cells with nanostructures in the oxide transport layer fully fabricated in air.

### 3.4. Investigation of the mechanism for improvement in efficiency

Characterization by UV–Vis absorbance, conductivity under illumination, morphology via AFM, Electrochemical Impedance Spectroscopy, and Photoluminescence via Time Correlated Single Photon Counting were used in order to understand the origin of the improvement in PCE after incorporating Ag nanoparticles from chemical synthesis.

As already mentioned, UV–Vis showed no detectable plasmonic effects from chemically synthesized Ag nanoparticles into the composite layer, probably due to their relatively low concentration in the thin SnO_2 layer ($\approx$25 nm). Conductivity measurements on the composite layers Ag NPs + SnO_2 are repeated under illumination to simulate the operation of solar cells, but also in this case the conductivity decreases with respect to

Table 1
PCE, V_{OC}, J_{SC}, FF, R_{SH}, and R_S of ITO/SnO_2(+Ag nanoparticles)/$CH_3NH_3PbI_3$/PTAA/Ag solar cells, as a function of the concentration of Ag nanoparticle solution with respect to SnO_2 solution. Both average and values of the best device are indicated. Best results in the literature for plasmonic perovskite solar cells fabricated in air are reported for comparison [41].

Ag NPs solution: SnO_2 solution	PCE (%)		V_{OC} (V)		J_{SC} (mA /cm^2)		FF (%)		R_{SH} ($\Omega \cdot cm^2$)	R_S ($\Omega \cdot cm^2$)
	Average	Best	Average	Best	Average	Best	Average	Best	Average	Average
0: 1 (no Ag NPs)	13.4 $\pm$ 0.7	14.41	1.01 $\pm$ 0.01	1.006	22.0 $\pm$ 0.4	22.63	60.2 $\pm$ 3.2	63.27	880 $\pm$ 650	9.4 $\pm$ 4.5
1: 1	13.8 $\pm$ 0.6	14.64	1.01 $\pm$ 0.01	1.024	21.8 $\pm$ 0.5	22.38	62.7 $\pm$ 2.3	63.85	1100 $\pm$ 1400	6.6 $\pm$ 0.8
2: 1	14.3 $\pm$ 0.3	14.87	1.02 $\pm$ 0.01	1.019	21.6 $\pm$ 0.3	21.87	65.1 $\pm$ 1.4	66.71	6600 $\pm$ 11000	6.2 $\pm$ 0.4
4: 1	14.1 $\pm$ 0.8	15.02	1.02 $\pm$ 0.01	1.028	21.1 $\pm$ 1.0	21.59	65.1 $\pm$ 2.1	67.67	1500 $\pm$ 1900	7.1 $\pm$ 0.8
Literature [41]	13.85 $\pm$ 0.45		0.995 $\pm$ 0.017		21.43 $\pm$ 1.01		64.3 $\pm$ 1.6			
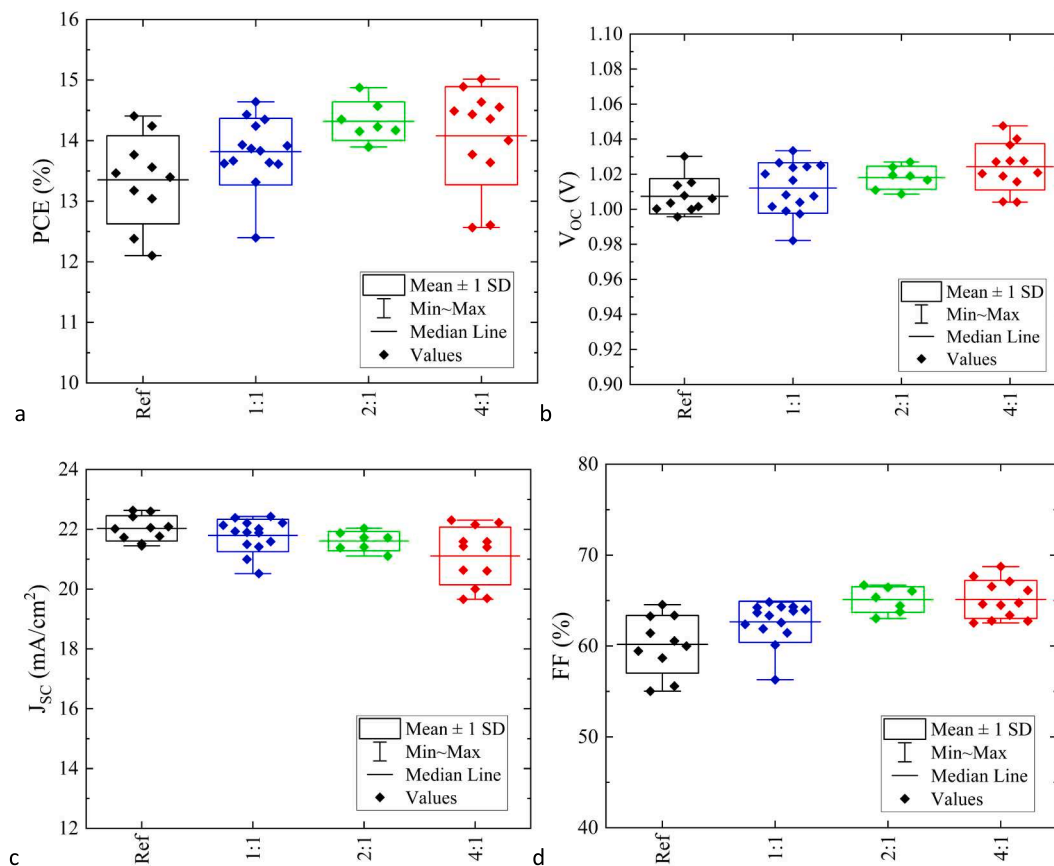
Fig. 3. Main parameters of solar cells. PCE (a), V_{OC} (b), J_{SC} (c), and FF (d) of ITO/SnO$_2$(+Ag nanoparticles)/CH$_3$NH$_3$PbI$_3$/PTAA/Ag solar cells, as a function of the concentration of Ag nanoparticle solution with respect to SnO$_2$ solution (DI H$_2$O balanced the dilution in order to reach always a total of 4 times the volume of SnO$_2$ solution).

bare SnO$_2$. AFM reported an increase of R_{RMS} roughness from 1.181 nm to 1.673 nm. Although this can improve the adhesion with perovskite layer and the extraction of electrons, other analyses are performed to better understand the effects of nanoparticles on the transport layer: EIS and photoluminescence.

Electrochemical Impedance Spectroscopy (EIS) is performed on full solar cells with transport layers formed of SnO$_2$ and Ag nanoparticles with different concentrations, in the dark with a bias of 0.9 V. Results are reported in the Nyquist plot (imaginary versus real part of impedance) in Fig. 4a. The results are modelled by applying the equivalent circuit indicated in the inset of Fig. 4a, and composed of a resistor R_1 in series with a parallel of a resistor R_2 and a capacitor C_2. The values of the fits are listed in Table 2; in one case two parallels of resistors and capacitors are required to have a good fit. In EIS, features at low frequency (100——1000 Hz) indicate slow electrical processes such as migration of ions; features at intermediate frequency (10 000——100 000 Hz) represent radiative and non radiative recombinations; and features at high frequency ($\geq$100 000 Hz) arise from fast mechanisms like charge transport and extraction.[48–52] In our experiments we detected arcs at intermediate frequencies, that can be interpreted as generated from the recombination mechanisms in solar cells, that have a typical time scale of $\approx$ μs. The characteristic times τ = R·C for the processes at intermediate frequencies are represented in Fig. 4b. With the increase of Ag nanoparticle concentration, τ decreases, that indicates that they accelerate the recombinations of charge carriers in the solar cell. This suggests that the Ag nanoparticles act as recombination centers for the electrons and holes present in the perovskite layer, detrimentally decreasing the number of charge carriers available to flow through the layer, that is the J_{SC} as reported in Fig. 3c, and consequently the global performance of the solar cell. A second effect of Ag nanoparticles is to

decrease the series resistance R_1 of SnO$_2$. The apparent contradiction with the decrease in conductivity after incorporation of Ag nanoparticles may be generated by the different geometries of analysis for the two techniques: parallel to the layer for 4 point probe measurements, and perpendicular to the layer for EIS. The presence of nanoparticles makes the conductivity anisotropic, because the electrons in the perovskite layer can move more easily across the ETL through the nanoparticles, although there are less electrons available along the ETL itself.

Time Correlated Single Photon Counting (TCSPC) is applied to study the photoluminescence of electron only devices, *i.e.*, with the architecture glass/SnO$_2$(+Ag nanoparticles)/CH$_3$NH$_3$PbI$_3$/encapsulation glass, for different concentrations of Ag nanoparticles. The normalized intensity spectra in Fig. 5a are fitted with 2 exponential decays ($I = I_0 + A_1 e^{-t/\tau_1} + A_2 e^{-t/\tau_2}$), as indicated by black lines with parameters listed in Table 3. In the literature, these multiple decays are ascribed to bimolecular mechanisms and free carrier mechanisms,[53] or to surface and bulk processes,[54,55] or to decays from different energy states. [56] By comparing the values of A_n in Table 3 the mechanism at shorter times, A_1, is the strongest for all the devices incorporating Ag nanoparticles, whereas the situation is more balanced for the reference device without Ag nanoparticles.[57] An effective lifetime τ_{EFF} that aggregates the different decay mechanisms,[54] according to the equation $1/\tau_{EFF} = 1/\tau_1 + 1/\tau_2$ is considered. Values are included in Table 3, and plotted in Fig. 5b.

This effective lifetime changes with the presence and the concentration of Ag nanoparticles. In perovskite solar cells with metal nanoparticles, this value is an indication of the characteristic time for the extraction of charge carriers through the transport layer. [14,41,45,47,58] As evident in Fig. 5b, the lifetime decreases with the concentration of Ag nanoparticles, from 1.223 ± 0.013 ns for reference

a

b
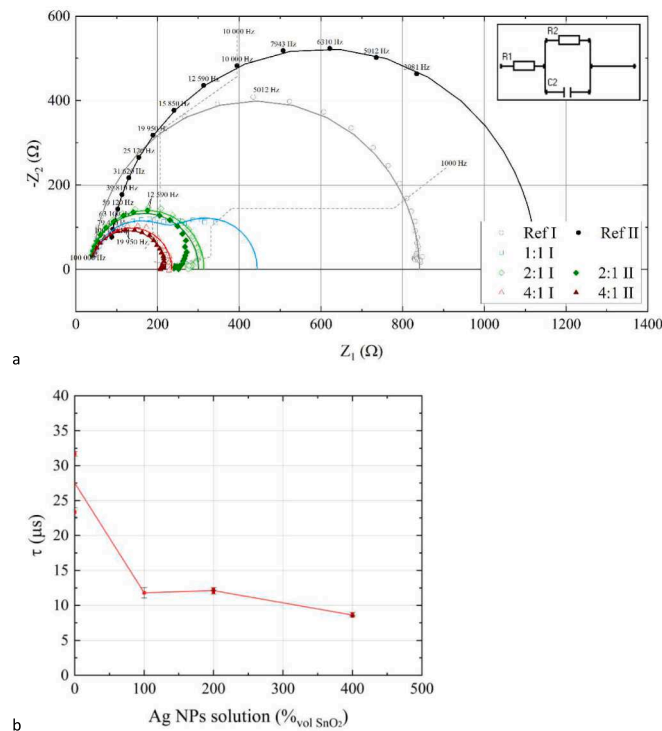
Fig. 4. Results from EIS. (a) Real Z_1 and imaginary -Z_2 components of the impedance in the Nyquist plot, for 8 solar cells ITO/SnO$_2$(+Ag nanoparticles)/CH$_3$NH$_3$PbI$_3$/PTAA/Au with different Ag nanoparticle concentrations, measured at 0.9 V in the darkness. Fits with the equivalent circuit in the inset are indicated by continuous lines. (b) Characteristic times τ = R·C of RC semicircles for solar cells as a function of the concentrations of Ag nanoparticles in the transport layer.

Table 2
Results of the EIS fits for solar cells measured at 0.9 V in the darkness: equivalent circuit for fitting, series resistance R_1, resistances $R_{2,3}$ and capacitances $C_{2,3}$ of the RC circuits.

Ag NPs solution: SnO$_2$ solution	Equivalent circuit	R_1 (Ω)	R_2 (Ω)	C_2 (nF)	R_3 (Ω)	C_3 (nF)
0: 1 (no Ag NPs)	R + RC	42.2 ± 0.6	799 ± 3	39.7 ± 0.3	–	–
0: 1 (no Ag NPs)	R + RC	82.2 ± 1.9	1050 ± 20	22.3 ± 0.2	–	–
1: 1	R + RC + RC	40.5 ± 1.4	193 ± 7	61.0 ± 1.6	210 ± 11	705 ± 71
2: 1	R + RC	33.4 ± 0.7	280 ± 2	43.9 ± 0.5	–	–
2: 1	R + RC	34.2 ± 0.8	266 ± 3	44.7 ± 0.5	–	–
4: 1	R + RC	37.8 ± 0.9	197 ± 2	44.4 ± 0.7	–	–
4: 1	R + RC	35.7 ± 0.5	185 ± 1	45.8 ± 0.4	–	–

SnO$_2$ to 0.744 ± 0.007 ns for Ag nanoparticles:SnO$_2$ ratio of 2:1. Therefore, the effect of Ag nanoparticles is to accelerate the extraction of charge carriers (electrons) from the perovskite to the transport layer. This improvement of electrical properties is supported also by the decrease of the series resistance R_1 detected in the EIS analyses, and by the minimum of the series resistance in perovskite solar cells happening at the same concentration of Ag nanoparticles:SnO$_2$ of 2:1. This positive effect on carrier extraction due to the Ag nanoparticles is in competition with the negative effect observed via EIS of increasing the recombination rate and decreasing the J_{SC}. Optimal conditions are met at

a

b
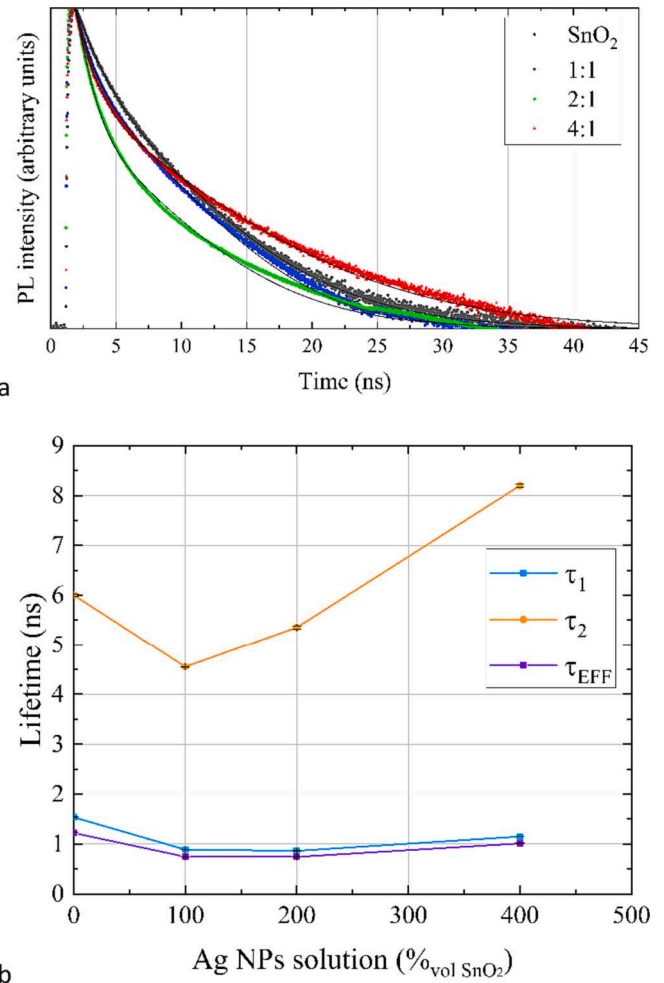
Fig. 5. Results from TCSPC. (a) Normalized intensity of PL emissions in logarithmic scale as a function of the time of emission, for samples composed of glass/SnO$_2$(+Ag nanoparticles)/CH$_3$NH$_3$PbI$_3$. Fits for each curve are plotted as black lines. The feature at 25 ns for 2:1 sample represents an artifact. (b) Lifetimes τ for the PL exponential decays as a function of the concentrations of Ag nanoparticles in the transport layer: first and second exponential decays, and effective lifetime.

Table 3
Fitting parameters of the PL emission curves ($I = I_0 + A_1 e^{-t/\tau_1} + A_2 e^{-t/\tau_2}$), for different concentrations of Ag nanoparticles in the transport layer.

Ag NPs solution: SnO$_2$ solution	I_0 (counts)	A_1 (counts)	τ_1 (ns)	A_2 (counts)	τ_2 (ns)	τ_{EFF} (ns)
0: 1 (no Ag NPs)	642 ± 3	9520 ± 50	1.536 ± 0.010	9770 ± 60	6.004 ± 0.024	1.223 ± 0.013
1: 1	1012 ± 8	67 200 ± 100	0.889 ± 0.003	41 900 ± 100	4.553 ± 0.013	0.744 ± 0.005
2: 1	10 260 ± 70	454 800 ± 900	0.864 ± 0.003	139 200 ± 900	5.352 ± 0.031	0.744 ± 0.007
4: 1	1053 ± 7	17 450 ± 50	1.152 ± 0.006	11 170 ± 40	8.197 ± 0.038	1.010 ± 0.010

intermediate concentrations, that in our system is Ag nanoparticles: SnO$_2$ 2:1, where the PCE of solar cells is maximum (Fig. 3a). This results in devices with a PCE of 14.3 ± 0.3 % for Ag nanoparticles in SnO$_2$

which is an improvement over the next best efficiency of 13.8 % reported for similar air processed devices incorporating nanoparticles. [41] Looking back to the thermally evaporated nanoparticles, it is possible to attribute the decrease in their efficiency to extensive carrier recombination mediated by nanoparticles, which is predominant at such excessive concentrations.

4. Conclusions

This work demonstrates how metal nanoparticles can be synthesized and optimized via chemical or physical methods, and subsequently how they can be integrated into the electron transport layer of perovskite solar cells. Different nanoparticle synthesis methods have different effects on perovskite solar cells: while thermally evaporated nanoparticles decreased the PCE, nanoparticles from chemical synthesis co-deposited with SnO_2 successfully increased the PCE by $+7$ %. A solution to the debate in the literature about the mechanism underlying the improvement in PCE has been proposed here: although the EIS reported an increase in recombination rates with increasing concentration of nanoparticles, photoluminescence highlighted that the characteristic time for charge transport decreased from 1.223 ± 0.013 ns to 0.744 ± 0.007 ns after incorporation of Ag nanoparticles into SnO_2. This can be interpreted as enhanced charge transfer and extraction from the perovskite layer into the electrode, that ultimately increased the PCE of the solar cells. The presence of these two opposing effects of extraction and recombination generates an optimal concentration of nanoparticles. The thermally evaporated nanoparticles could only be made at concentrations above optimum, whereas the concentration of the chemically derived nanoparticles could be tuned and therefore optimized. In comparison to other works in the literature, this work is the first to apply metal nanoparticles in SnO_2, one of the most efficient ETLs for perovskite solar cells. Additionally, our solar cells are some of the first to be fabricated completely in air incorporating a composite metal nanoparticle/oxide electron transport layer, and with the highest reported PCE for this material system. In conclusion, perovskite solar cells have been enhanced in terms of improved efficiency and simple processing, *i. e.*, without the need for expensive control of the processing environment. Understanding of the mechanisms by which nanoparticles enhance device performance has been improved. Lastly, the protocols established here for the synthesis, comparison and integration of composite transport layers have a general validity, and can be applied to perovskite solar cells with different compositions, or to other fields, *e.g.*, LED, FET, and fuel cells.

Declaration of competing interest

The authors declare that they have no known competing financial interests or personal relationships that could have appeared to influence the work reported in this paper.

Acknowledgements

References

[1] A. Kojima, K. Teshima, Y. Shirai, T. Miyasaka, J. Am. Chem. Soc. 131 (2009) 6050–6051.

[2] National Renewable Energy Laboratory, Best Research-Cell Efficiency Chart, https://www.nrel.gov/pv/assets/images/efficiency-chart.png.

[3] N.G. Park, Mater. Today 18 (2015) 65–72.

[4] G. Giorgi, K. Yamashita, J. Mater. Chem. A 3 (2015) 8981–8991.

[5] S. Luo, W.A. Daoud, J. Mater. Chem. A 3 (2015) 8992–9010.

[6] B.G. Krishna, D. Sundar Ghosh, S. Tiwari, Sol. Energy 224 (2021) 1369–1395.

[7] G. Niu, X. Guo, L. Wang, J. Mater. Chem. A 3 (2015) 8970–8980.

[8] L. Calió, S. Kazim, M. Grätzel and S. Ahmad, Angew. Chem. – Int. Ed., 2016, 55, 14522–14545.

[9] Z. Song, J. Liu, G. Wang, W. Zuo, C. Liao, J. Mei, ChemPhysChem 18 (2017) 3030–3038.

[10] M.L. Petrus, M.T. Sirtl, A.C. Closs, T. Bein, P. Docampo, Mol. Syst. Des. Eng. 3 (2018) 734–740.

[11] M.L. Petrus, T. Bein, T.J. Dingemans, P. Docampo, J. Mater. Chem. A 3 (2015) 12159–12162.

[12] S. Valero, S. Collavini, S. F. Völker, M. Saliba, W. R. Tress, S. M. Zakeeruddin, M. Grätzel and J. L. Delgado, Macromolecules, 2019, 52, 2243–2254.

[13] M. Stavytska-Barba, M. Salvador, A. Kulkarni, D.S. Ginger, A.M. Kelley, J. Phys. Chem. C 115 (2011) 20788–20794.

[14] Z. Lu, X. Pan, Y. Ma, Y. Li, L. Zheng, D. Zhang, Q. Xu, Z. Chen, S. Wang, B. Qu, F. Liu, Y. Huang, L. Xiao, Q. Gong, RSC Adv. 5 (2015) 11175–11179.

[15] Y. Liu, F. Lang, T. Dittrich, A. Steigert, C. H. Fischer, T. Köhler, P. Plate, J. Rappich, M. C. Lux-Steiner and M. Schmid, RSC Adv., 2017, 7, 1206–1214.

[16] Z. Yuan, Z. Wu, S. Bai, Z. Xia, W. Xu, T. Song, H. Wu, L. Xu, J. Si, Y. Jin, B. Sun, Adv. Energy Mater. 5 (2015) 1500038.

[17] C. Zhang, Q. Luo, J. Shi, L. Yue, Z. Wang, X. Chen, S. Huang, Nanoscale 9 (2017) 2852–2864.

[18] R. Siavash, Moakhar, S. Gholipour, S. Masudy-Panah, A. Seza, A. Mehdikhani, N. Riahi-Noori, S. Tafazoli, N. Timasi, Y.F. Lim, M. Saliba, Adv. Sci. 7 (2020) 1–19.

[19] M. Gu, Z. Ouyang, B. Jia, N. Stokes, X. Chen, N. Fahim, X. Li, M.J. Ventura, Z. Shi, Nanophotonics 1 (2012) 235–248.

[20] S. Woo, J. Jeong, H. Lyu, Y. Han, Y. Kim, Nanoscale Res. Lett. 7 (2012) 641.

[21] X. Li, Z. Deng, Y. Yin, L. Zhu, D. Xu, Y. Wang, F. Teng, J. Mater. Sci. Mater. Electron. 25 (2014) 140–145.

[22] E. Stratakis, E. Kymakis, Mater. Today 16 (2013) 133–146.

[23] H. Min, D.Y. Lee, J. Kim, G. Kim, K.S. Lee, J. Kim, M.J. Paik, Y.K. Kim, K.S. Kim, M. G. Kim, T.J. Shin, S. Il Seok, Nature 598 (2021) 444–450.

[24] M. Rycenga, C.M. Cobley, J. Zeng, W. Li, C.H. Moran, Q. Zhang, D. Qin, Y. Xia, Chem. Rev. 111 (2011) 3669–3712.

[25] A. Kumar, S. Rani, N.K. Rana, M.R. Samantaray, N. Chander, D.S. Ghosh, Sol. Energy 244 (2022) 457–464.

[26] S. Rani, A. Kumar and D. S. Ghosh, Materials Today: Proceedings, in press (Effect of rate of deposition on opto-electrical characteristics of vapor deposited MoO3/Ag/MoO3 transparent electrode for photovoltaic applications).

[27] L. Mulfinger, S.D. Solomon, M. Bahadory, A.V. Jeyarajasingam, S.A. Rutkowsky, C. Boritz, J. Chem. Educ. 84 (2007) 322.

[28] Q. Jiang, Y. Zhao, X. Zhang, X. Yang, Y. Chen, Z. Chu, Q. Ye, X. Li, Z. Yin, J. You, Nat. Photonics 13 (2019) 460–466.

[29] Q. Jiang, L. Zhang, H. Wang, X. Yang, J. Meng, H. Liu, Z. Yin, J. Wu, X. Zhang, J. You, Nat. Energy 2 (2016) 1–7.

[30] N.J. Jeon, J.H. Noh, Y.C. Kim, W.S. Yang, S. Ryu, S.I. Seok, Nat. Mater. 13 (2014) 897–903.

[31] J. Troughton, K. Hooper, T.M. Watson, Nano Energy 39 (2017) 60–68.

[32] K.G. Stamplecoskie, J.S. Manser, P.V. Kamat, Energ. Environ. Sci. 8 (2015) 208–215.

[33] K. Tsevas, J.A. Smith, V. Kumar, C. Rodenburg, M. Fakis, A.R.B. Mohd Yusoff, M. Vasilopoulou, D.G. Lidzey, M.K. Nazeeruddin, A.D. Dunbar, Chem. Mater. 33 (2021) 554–566.

[34] J.H. Heo, M.H. Lee, H.J. Han, B.R. Patil, J.S. Yu, S.H. Im, J. Mater. Chem. A 4 (2016) 1572–1578.

[35] J.H. Heo, H.J. Han, D. Kim, T.K. Ahn, S.H. Im, Energ. Environ. Sci. 8 (2015) 1602–1608.

[36] S. Ryu, J. Seo, S.S. Shin, Y.C. Kim, N.J. Jeon, J.H. Noh, S.I. Seok, J. Mater. Chem. A 3 (2015) 3271–3275.

[37] F. Bastianini and A. Dunbar, 14th Photovoltaic Science, Applications and Technology Conference PVSAT-14, 2018, 101–104.

[38] D. Barreca, A. Gasparotto, E. Tondello, G. Bruno, M. Losurdo, J. Appl. Phys. 96 (2004) 1655–1665.

[39] A.K. Mohamedkhair, Q.A. Drmosh, Z.H. Yamani, Front. Mater. 6 (2019) 1–10.

[40] A. Kolmakov, D.O. Klenov, Y. Lilach, S. Stemmer, M. Moskovitst, Nano Lett. 5 (2005) 667–673.

[41] F. Qi, C. Wang, N. Cheng, P. Liu, Y. Xiao, F. Li, X. Sun, W. Liu, S. Guo, X.Z. Zhao, Electrochim. Acta 282 (2018) 10–15.

[42] W. Zhang, M. Saliba, S.D. Stranks, Y. Sun, X. Shi, U. Wiesner, H.J. Snaith, Nano Lett. 13 (2013) 4505–4510.

[43] S.Y. Abate, W.T. Wu, S. Pola, Y.T. Tao, RSC Adv. 8 (2018) 7847–7854.

[44] B. Wang, X. Zhu, S. Li, M. Chen, H. Lu, Y. Yang, Nanomaterials 8 (2018) 1–15.

[45] J. Du, Y. Zhang, M. Yang, D. Han, L. Fan, Y. Sui, J. Yang, L. Yang, F. Wang, ACS Appl. Mater. Interfaces 12 (2020) 41446–41453.

[46] M. Saliba, W. Zhang, V.M. Burlakov, S.D. Stranks, Y. Sun, J.M. Ball, M.B. Johnston, A. Goriely, U. Wiesner, H.J. Snaith, Adv. Funct. Mater. 25 (2015) 5038–5046.

[47] H. Dong, T. Lei, F. Yuan, J. Xu, Y. Niu, B. Jiao, Z. Zhang, D. Ding, X. Hou, Z. Wu, Org. Electron. 60 (2018) 1–8.

[48] C.H. Ng, H.N. Lim, S. Hayase, Z. Zainal, N.M. Huang, Renew. Sustain. Energy Rev. 90 (2018) 248–274.

[49] S. Ali, S. Chang, M. Imran, Q. Shi, Y. Chen, H. Zhong, Physica Status Solidi – Rapid Research Letters 13 (2019) 1–16.

[50] H. Wang, A. Guerrero, A. Bou, A.M. Al-Mayouf, J. Bisquert, Energ. Environ. Sci. 12 (2019) 2054–2079.

[51] P. Lopez-Varo, J.A. Jiḿenez-Tejada, M. Garćia-Rosell, S. Ravishankar, G. Garcia-Belmonte, J. Bisquert, O. Almora, Adv. Energy Mater. 8 (2018) 1–36.

[52] A. Todinova, L. Contreras-Bernal, M. Salado, S. Ahmad, N. Morillo, J. Idıgoras and J. J. a. Anta, ChemElectroChem 4 (2017) 2891–2901.

[53] Q. Chen, H. Zhou, T.B. Song, S. Luo, Z. Hong, H.S. Duan, L. Dou, Y. Liu, Y. Yang, Nano Lett. 14 (2014) 4158–4163.

[54] F. Staub, H. Hempel, J.C. Hebig, J. Mock, U.W. Paetzold, U. Rau, T. Unold, T. Kirchartz, Phys. Rev. Appl 6 (2016) 1–13.

[55] P. Chen, Y. Bai, S. Wang, M. Lyu, J.H. Yun, L. Wang, Adv. Funct. Mater. 28 (2018) 1–10.

[56] Y. Chen, T. Wang, Z. Li, H. Li, T. Ye, C. Wetzel, H. Li, S.F. Shi, Sci. Rep. 8 (2018) 1–7.

[57] X. Hu, X. Wang, P. Fan, Y. Li, X. Zhang, Q. Liu, W. Zheng, G. Xu, X. Wang, X. Zhu, A. Pan, Nano Lett. 18 (2018) 3024–3031.

[58] H.A. Atwater, A. Polman, Nat. Mater. 9 (2010) 205–213.